

An Atomically Thin Optoelectronic Machine Vision Processor


Houk Jang, Chengye Liu, Henry Hinton, Min-Hyun Lee, Haeryong Kim, Minsu Seol, Hyeon-Jin Shin, Seongjun Park,* and Donhee Ham*

2D semiconductors, especially transition metal dichalcogenide (TMD) monolayers, are extensively studied for electronic and optoelectronic applications. Beyond intensive studies on single transistors and photodetectors, the recent advent of large-area synthesis of these atomically thin layers has paved the way for 2D integrated circuits, such as digital logic circuits and image sensors, achieving an integration level of ≈ 100 devices thus far. Here, a decisive advance in 2D integrated circuits is reported, where the device integration scale is increased by tenfold and the functional complexity of 2D electronics is propelled to an unprecedented level. Concretely, an analog optoelectronic processor inspired by biological vision is developed, where $32 \times 32 = 1024$ MoS₂ photosensitive field-effect transistors manifesting persistent photoconductivity (PPC) effects are arranged in a crossbar array. This optoelectronic processor with PPC memory mimics two core functions of human vision: it captures and stores an optical image into electrical data, like the eye and optic nerve chain, and then recognizes this electrical form of the captured image, like the brain, by executing analog in-memory neural net computing. In the highlight demonstration, the MoS₂ FET crossbar array optically images 1000 handwritten digits and electrically recognizes these imaged data with 94% accuracy.

2D semiconductors, in particular transition metal dichalcogenide (TMD) monolayers, have taken the nano and condensed matter research communities by storm over the past decade.^[1–3] Having direct bandgaps, these atomically thin materials are suitable for electronic and optoelectronic works, with their stacks into various heterostructures promising a wealth of engineered electronic and optoelectronic properties.^[3–8] While single transistors and photodetectors built from 2D materials have already garnered significant research interest,^[9–12] recent advances in large-area synthesis of TMD monolayers have opened up an exciting possibility to integrate a large number

Dr. H. Jang, Dr. C. Liu, H. Hinton, Prof. D. Ham
School of Engineering and Applied Sciences
Harvard University
Cambridge, MA 02138, USA
E-mail: donhee@seas.harvard.edu

Dr. M.-H. Lee, Dr. H. Kim, Dr. M. Seol, Dr. H.-J. Shin, Dr. S. Park
Samsung Advanced Institute of Technology
Samsung Electronics
Suwon 443-803, South Korea
E-mail: s3.park@samsung.com

 The ORCID identification number(s) for the author(s) of this article can be found under <https://doi.org/10.1002/adma.202002431>.

DOI: 10.1002/adma.202002431

of devices into circuits.^[13–15] Notable recent examples in this direction of 2D integrated circuits (ICs) include an image sensor with 48 molybdenum disulfide (MoS₂) photoconductors^[16] and digital logic circuits^[17,18] integrating as many as 115 MoS₂ field-effect transistors (FETs).^[19]

In this article, we expand the functional complexity of 2D ICs through a tenfold increase in the device integration scale. Specifically, we have developed an analog optoelectronic processor comprised of 1024 (32×32) MoS₂ photo-FETs arranged in a crossbar array structure. Through capturing of optical images into electrical data (like the eye and optic nerve), and subsequent recognition of this data (like the brain) via analog in-memory computing, our optoelectronic processor emulates the two core functions of human vision (Figure 1a).

For the front-end optical image sensing, the crossbar array is operated as an active pixel sensor array. Our MoS₂ FETs manifest photoconductivity that persists even after light removal. With this persistent photo conductivity (PPC)^[20–23] serving as an optoelectronic memory, the array captures and stores an input optical scene into electrical data (FET conductance values) with the image resolution far higher than the prior TMD image sensor with 48 pixels.^[16] For the back-end recognition of this acquired image, we recycle the crossbar array to perform analog convolutional neural network (CNN) computing. To this end, we optically program new FET conductance values, representing the synaptic weight values of the CNN, into the crossbar array with the PPC imaging method above. The electrically converted scene data from the front-end optical image sensing are then fed as a vector into this updated crossbar array, which executes vector–matrix multiplications, the canonical CNN operation, in an analog manner to recognize the image. We demonstrate the operation of our optoelectronic analog machine vision processor for 1000 handwritten digits from the Modified National Institute of Standards and Technology (MNIST) database with 94% accuracy.

Analog machine vision has been actively pursued by various material systems beyond 2D materials. Most notably, crossbar arrays of oxide memristors or phase-change memories,^[24–29] which act as analog vector–matrix multiplication engines, have profoundly shaped the field of analog neural network computing for back-end image recognition, overcoming the large

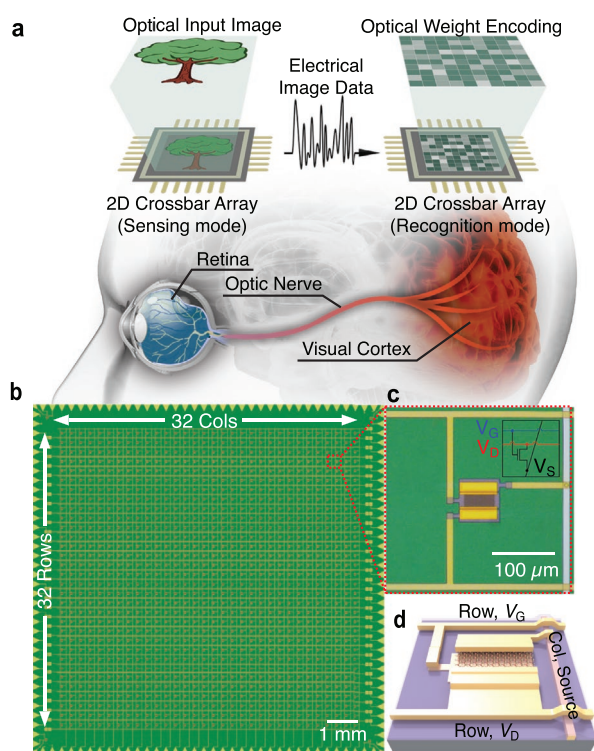


Figure 1. MoS₂ photo-FET crossbar array as an analog optoelectronic machine vision processor. a) Our MoS₂ optoelectronic processor mimics two core functions of the human vision system: front-end image sensing, like the retina and optic nerve, and back-end recognition, like the brain. b,c) Optical microscopy images of the 32 × 32 MoS₂ photo-FET crossbar array (b) and of a unit pixel (c). The inset shows a schematic of the unit pixel, or cross point conductor. d) 3D rendering of the interconnect arrangement for a single pixel.

power budget of the otherwise enormously successful digital neural net paradigm. At the same time, various material systems, including organics and perovskites, have been employed to develop front-end in-memory image sensors,^[30–34] so far integrating up to 100 pixels. Our 2D crossbar array brings together front-end optical image sensing (with high-resolution and full-frame readout) and back-end image recognition (via analog in-memory computing) in a unified material platform, exploiting all necessary electronic, optoelectronic, and memory traits available to the 2D semiconducting material, thereby advancing the pursuit toward integrated analog machine vision.

Figure 1b shows the fabricated 32 × 32 array of *n*-FETs using a large-area MoS₂ monolayer synthesized by metal–organic chemical vapor deposition (MOCVD) (see Method S1 and Figure S1, Supporting Information, for more detailed information on the synthesized monolayer MoS₂; and see Figure 1b and Method S2, Supporting Information, for the detailed fabrication process). The length and width of each FET channel are 20 and 50 μm, respectively (Figure 1c). Each FET has a back gate in lieu of a top gate so that its channel can be exposed to light from above (Figure 1d). 32 metal (90 nm Au, 10 nm Cr) row lines contact the FETs' drain nodes and 32 metal column lines contact the FETs' source nodes, both from below the MoS₂ layer. Each FET channel thus serves as a cross-point conductor

between its row (drain) and column (source) lines (inset of Figure 1c). Another set of 32 metal row lines tap the FETs' back gates for biasing. The overall crossbar circuit schematic is in Figure S2a, Supporting Information.

This crossbar array of photo-FETs is used first as a front-end optical image sensor and is then reused, after re-initialization, for analog vector–matrix multiplications for back-end image recognition (Figure 1a). In the image sensing mode, the input scene, stored as FET conductance values via PPC, is read out row by row. At each read cycle, we positively bias only 1 drain row to activate the 32 FETs connected to it, with the remaining 31 drain rows connected to ground (all source nodes are at virtual ground; Figure S2b, Supporting Information), and measure column currents. Each column current is then from a single FET at the cross point of that column and the activated drain row. We repeat this procedure through 32 read cycles, sequentially activating each row and measuring column currents. In this way, we can measure the channel conductance of all FETs with an effective frame readout time of ≈1 s.

Vector–matrix multiplications for the back-end image recognition mode are analog, or physical, operations based on Ohm's and Kirchhoff's laws: If, for example, the entire array is used as an FET conductance matrix and all the drain rows are fed with voltages, the resulting 32 column currents, or the 1 × 32 column current vector, is the dot product of the transpose of the 32 × 1 drain row voltage vector and the 32 × 32 conductance matrix (Figure S2c, Supporting Information). This simple analog vector–matrix multiplication, consisting of applying the input row voltages and recording the output column currents, contrasts the complex digital vector–matrix multiplication that involves many multiply-and-accumulate operations and consumes far more power. For this reason, such analog vector–matrix multiplication has been a key pursuit in neural network acceleration, notably with crossbar arrays of oxide or phase change memristors.^[24,25,29] It is this analog matrix multiplication that we expand to the 2D PPC memory crossbar array in this work.

The crossbar array chip is packaged and mounted on a custom-designed printed circuit board (PCB), which hosts auxiliary electronics such as digital-to-analog converters (DACs) to provide voltage inputs and biases to the drain and gate rows, and analog-to-digital converters (ADCs) to collect column currents (Method S3 and Figure S3, Supporting Information). The crossbar array and PCB electronics are programmed and automated together. By operating the crossbar array in the image sensing mode but with no light, we characterize the electrical performance of all 1024 FETs. 946 FETs work properly while 78 fail (yield: 92%). For the 946 working FETs, the on/off ratio is ≈10⁴, the threshold voltage is 0.02 ± 0.23 V, and the mobility is about 1 cm² V⁻¹ s⁻¹, as is typical with chemically synthesized MoS₂ monolayers (Figure S4, Supporting Information).

Figure 2a shows the measured channel photocurrent (*I*_{ph})—the overall current minus the bias (dark) current—from an example MoS₂ *n*-FET in the array, where a 1.4 W m⁻², 532 nm light is illuminated for 1 min. Here, the FET is biased with a gate voltage *V*_G of -6 V, a drain voltage *V*_D of 0.3 V, and a source voltage *V*_S of 0 V, which places the FET in the subthreshold region, exhibiting a bias current of a few hundred pA (Figures S4a and S5, Supporting Information; in both the image

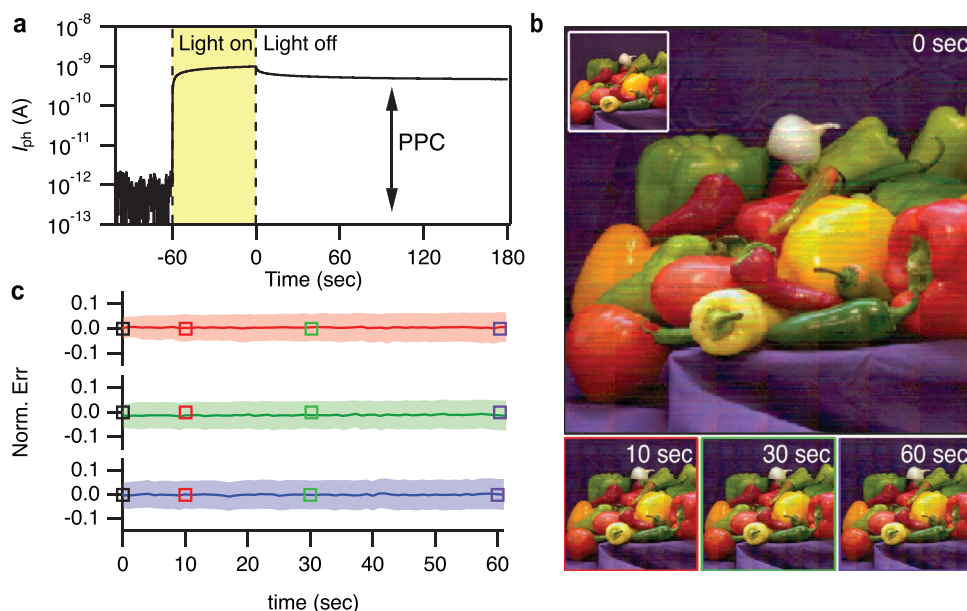


Figure 2. High-resolution, full-frame, front-end optical image sensing with PPC. a) The photocurrent ($I_{\text{ph}} = I - I_{\text{dark}}$) of an MoS₂ FET measured at $V_{\text{D}} = 0.3$ V, $V_{\text{G}} = -6$ V, and $V_{\text{S}} = 0$ V for 4 min, with the light (532 nm, 1.4 W m^{-2}) illuminated for the first 1 min. b) 240×240 calibrated composite image captured with peak photocurrents at $t = 0$ s after 5 s exposure to the “peppers” input image of the inset (top) and with PPC currents at $t = 10, 30, 60$ s (bottom) after closing the shutter at $t = 0$ s. c) The average (solid) and standard deviation (shaded) of the normalized pixel intensity difference between the captured and input image across $886 \text{ pixels} \times 64$ segments for each RGB color channel as a function of time after closing the shutter. Time points corresponding to the images in (b) are indicated by squares.

sensing mode described here and the image recognition mode presented later, we use subthreshold biasing for low-power operation). When exposed to light, the channel current rises from its bias value (the measured responsivity and detectivity are as large as 150 A W^{-1} and 1.1×10^{10} Jones, depending on the bias: Text S1 and Figure S6, Supporting Information). After light removal, the photocurrent (≈ 500 pA) decays very slowly (Text S2, Supporting Information),^[20,35] with an extrapolation predicting that $\approx 20\%$ of the peak photocurrent would remain after 10 years (Figure S7, Supporting Information). This is because much of the photoexcited carriers remain trapped at defect and impurity sites in the FET channel to reduce its threshold voltage.^[22,23,36] We can electrically erase this PPC memory, or prolonged photogating, by applying ≈ 7 V to the FET gate to remove the trapped carriers (see Text S2 and Figure S8, Supporting Information).^[12,21,37]

The front-end image sensing exploits this PPC memory at the array scale to acquire and store an optical image as electrical data (FET conductance values). Since most of the 78 FET failures are concentrated in two rows due to interconnect issues, we do not use these two rows, and to capture the image in a square frame, we also omit the use of two functioning columns. We hence capture an image using the 30×30 array with 886 working pixels and 14 dead pixels. To read out the captured image, we measure the channel currents of all array FETs by sequentially applying 0.1 V to each drain row for ≈ 2 ms with the remaining drain rows set at 0 V (V_{G} and V_{S} are at -6 V and 0 V for all FETs) and recording the column currents. A single scan of the entire frame then takes 60 ms. We repeat this scan multiple times to improve the image quality via averaging, resulting in the effective full-frame readout time of ≈ 1 s.

Figure 2b shows an example image sensing result. The input image of the inset of Figure 2b is divided into 64 segments,

and each segment is imaged by the crossbar array. After projecting a given segment image onto the 30×30 array for 5 s with a given color filter (blue, green, or red), we read out the captured image at every ≈ 1 s, starting from the moment we close the projector shutter ($t = 0$). Then till $t = 60$ s, we read 60 images stored in the array. This 65 s procedure is repeated for each of the 3 color filters, generating 60 images for each color. We then combine three different color images at each frame time, t , to produce a composite color image at that time t . Note that before starting the 65 s procedure for a new color, we electrically erase PPC memories from the previous color imaging. The image read out at $t = 0$ s (Figure 2b, top) is from the peak photocurrents, whereas the images read out at $t = 10, 30,$ and 60 s (Figure 2b, bottom) are the ones stored in the PPC memory array. It is apparent from Figure 2b that these stored images remain consistent over the course of time. This consistency is quantitatively verified in Figure 2c; the standard deviation of the normalized pixel intensity difference between the captured and input image across the $886 \text{ pixels} \times 64$ segments for each RGB color channel stays within 7% for all 60 time frames, without noticeable variation.

The variation of the FET mobilities and threshold voltages across the array (Figure S4b, Supporting Information) results in appreciable pixel-to-pixel photo response variations. These effects have already been calibrated out in the images of Figure 2b, where such calibration is routinely performed in the complementary metal-oxide semiconductor image sensors in consumer electronics as well. For the calibration procedure, see Method S4 and Figure S9, Supporting Information. Finally, in the images of Figure 2b, for each of the 14 dead pixels in the 30×30 array, we interpolate using the calibrated intensities from the neighboring pixels.

For the back-end image recognition, the crossbar array is used as an FET conductance matrix. We optically encode FET conductance values as desired matrix elements (e.g., synaptic weights), using the PPC image sensing technique described above. The conductance of each FET can be increased toward a desired value by increasing the cumulative light dosage, which is determined by the exposure time and light intensity (Figure S10, Supporting Information). This PPC increase can be done in a piecewise manner, by repeating the cycle of a short illumination and a PPC measurement (Figure S11, Supporting Information). Since the n -FET conductance can only increase with light, such iteration with the fine control over the light duration and intensity is helpful to obtain a desired FET conductance without overshoot. This iterative encoding is performed simultaneously across all pixels by exposing the

array to a composite image of different pixel light at each iteration cycle (Method S5, Supporting Information). Figure 3a shows an example of such iterative optical encoding across for four MoS₂ FETs in the array to drive them into four different well-defined conductance states after ≈ 40 iteration cycles (Figure 3a, inset). Using this image-based, array-wide iterative optical encoding, we can program the crossbar array into a desired matrix for analog vector–matrix multiplication.

Before demonstrating the CNN-based image recognition involving a more complex sequence of analog vector–matrix multiplications, we first assess the accuracy of the optical programming and the analog matrix multiplication by performing relatively simple image filtering tasks.^[24] To this end, we first use the crossbar array in the image sensing mode to capture a 120×120 grayscale image of the “cameraman” into the FET

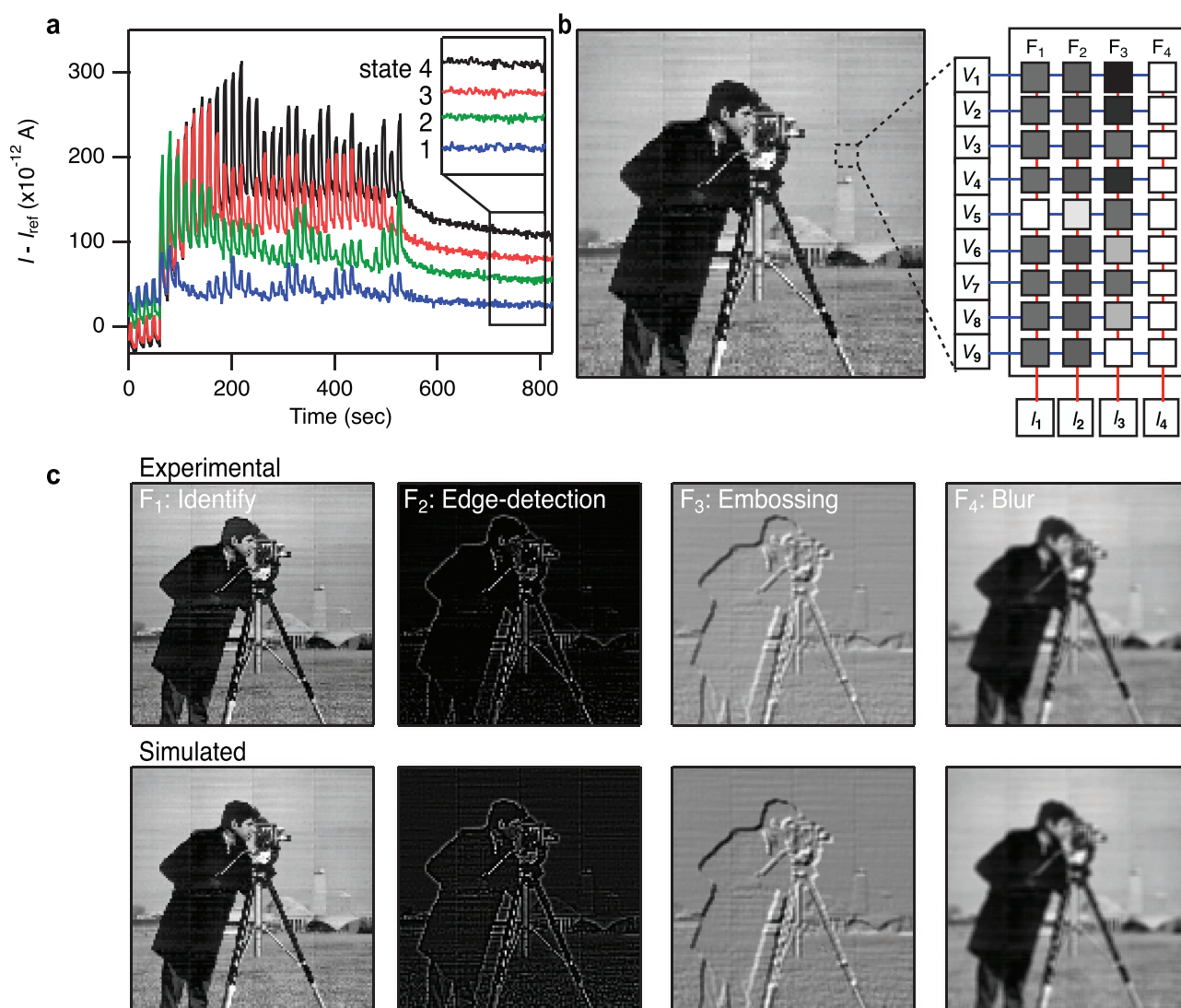


Figure 3. Optical programming of the conductance matrix and its application in image filtering. a) Iterative programming of four pixels. Their FET currents relative to the reference pixel ($I - I_{ref}$) are plotted with time. The reference pixel is not exposed during encoding to establish a baseline conductance. b) 120×120 calibrated composite “cameraman” image captured with peak photocurrents at $t = 0$ s after 5 s exposure (left) and schematic illustration of the image filtering with the 9×4 conductance matrix (four filters) in the crossbar array. The cameraman test image in (b) and (c) is used with permission from MIT. c) Four measured filtered images (top)—identity, edge-detection, embossing, and blur—and four simulated filtered images (bottom).

conductance values (Figure 3b, left, which is the image captured at $t = 0$; see Figure S12, Supporting Information, for the images stored up to $t = 60$ s). Subsequently, after saving the image data, we electrically reinitialize the array and optically encode a 9×4 portion of the crossbar array into a conductance matrix (Figure 3b, right). The four columns of this 9×4 matrix represent four independent filters: identity (F_1), edge-detection (F_2), embossing (F_3), and normalized blur (F_4) (Figure S13a, Supporting Information). Then, we choose a 3×3 conductance patch from the camera man image data (Figure 3b, left, dashed line) and convert it into a 9×1 voltage vector (V_1 to V_9 in Figure 3b). This 9×1 voltage vector is then fed to the 9×4 conductance matrix for analog vector–matrix multiplication, resulting in four column currents (I_1 to I_4 in Figure 3b). By sliding the 3×3 patch across 120×120 image frame and repeating the vector–matrix multiplication described above, we obtain a 118×118 matrix for each of I_1 through I_4 . These four 118×118 current matrices (Figure 3c) are the outcomes of convolving the four analog filter kernels with the captured image (Method S6, Supporting Information). Upon inspection, they apparently show identity, detected edges, embossing, and blurriness. To be more quantitative, we compare these filtering results from the analog vector–matrix multiplications to the simulated filtering results, which are the digital vector–matrix multiplications with the target filter values (Figure S13b, Supporting Information). For all four tests, the Pearson correlation coefficient of the simulated and experimental outputs exceeds 0.97 (Figure S13c, Supporting Information). This attests to the accuracy in both the optical encoding and the analog vector–matrix multiplications.

We now demonstrate the image sensing and recognition of 1000 hand-written digits from the MNIST database (100 hand-written shapes for each digit of “0” through “9”). We first capture the 1000 hand-written digit images by operating the crossbar array in the image sensing mode, with each captured electrical image data (FET conductance values) having a size 13×13 . See Figure S14, Supporting Information, for ten captured image examples (one for each digit).

Subsequently, we operate the crossbar array as a matrix multiplication engine to recognize any one of these 1000 imaged shapes, which we describe using the captured image “3” of Figure 4a as an example. To this end, after saving the imaged handwritten digit data, we electrically erase the PPC memories and optically program a 16×10 conductance matrix that represents a convolutional layer of the CNN, where we obtain the desired matrix element values from the off-line learning in the software domain (Method S7, Supporting Information). This 16×10 matrix represents ten convolutional filters, each sized 16×1 (their 4×4 versions are shown in Figure 4a,b). Then, we choose a 4×4 patch in the acquired 13×13 conductance-valued image for the digit “3” and convert it into a 16×1 voltage vector. This 16×1 voltage vector is fed to the 16×10 conductance matrix for the analog vector–matrix multiplication, resulting in 10 column currents (Figure 4a, blue dashed line). As we repeat the above process by sliding the 4×4 patch throughout the 13×13 MNIST digit “3” image data and collect the ten column currents each time, we generate ten 10×10 current-valued matrices or feature maps (Figure 4a, red dashed line and Figure 4c; see Method S6, Supporting Information).

As the next step, these ten 10×10 current-valued feature maps are down-sampled in the software max-pooling layer and converted into a 40×1 voltage vector. We then once again reinitialize the crossbar array and optically program a 40×10 conductance matrix as a fully connected layer of the CNN (again, we obtain the desired matrix elements from software learning, see Method S7, Supporting Information). As we feed the down-sampled 40×1 voltage vector into this 40×10 conductance matrix (because the 40×10 matrix does not directly fit into the 32×32 crossbar array, we split it to two 20×10 matrices, and we also accordingly split the input 40×1 voltage vector), the analog vector–matrix multiplication results in 10 column currents. These 10 column currents, along with their soft-maxed outputs that represent the Bayesian probabilities for all digits, inform the decision that the image belongs to the digit “3” (Figure 4d).

The above analog CNN computation with the example of the captured image “3” is repeated for each of the 1000 captured images. Ten feature map examples for each digit are shown in Figure S15a, Supporting Information. With 100 different images for each digit, we calculate the correlation coefficient between the feature maps generated using the target weight array and the feature maps simulated using the target weight values; the average of the resulting 10 correlation coefficients exceeds 0.98 (Figure S15b, Supporting Information). Figure S16, Supporting Information, shows outputs of the fully connected layer for 10 example digit shapes. Finally, Figure 4e shows the statistics of the experimental decisions for the 1000 digit images, which reaches 94% accuracy in the image classification.

In our recognition process, the crossbar matrix subarrays execute 31 790 analog arithmetic operations (addition and multiplication) per input image and consume an average power of only $\approx 1.65 \mu\text{W}$. This calculation is to provide a sense of the low power consumption of the analog neural net computing on the 2D FET crossbar subarray, so the power cost of peripheral electronics such as the ADCs and DACs is not included.

In summary, we have developed an atomically thin optoelectronic machine vision processor by integrating 1024 MoS₂ photo-FETs with PPC memory in a crossbar structure—the largest scale IC to date in TMD-based electronics. As a front-end image sensor, this crossbar array acquires and stores an input optical scene in the form of FET PPC values. For the back-end recognition of this acquired image, the crossbar array is optically programmed with new conductance values representing the synaptic weights of the neural net matrices, and then this programmed crossbar array executes analog voltage-vector–conductance-matrix multiplication to recognize the image. Such analog matrix multiplication is an active pursuit in achieving low-power neural network operation, and our work demonstrates this analog in-memory computation with the largest 2D crossbar array to date, enabling high-level tasks, such as image recognition. Mimicking two core functions of the human vision system, this processor visually recognized 1000 handwritten digits with an accuracy of 94%, highlighting an unprecedented advance in the functional complexity of 2D electronics. Overall, our work demonstrates the application of 2D materials in building large-scale in-memory sensor arrays as well as non-von-Neuman analog in-memory computing systems. The circuit presented in this work can be readily modified and expanded to new architectures for a variety of sensing and analog computing tasks.

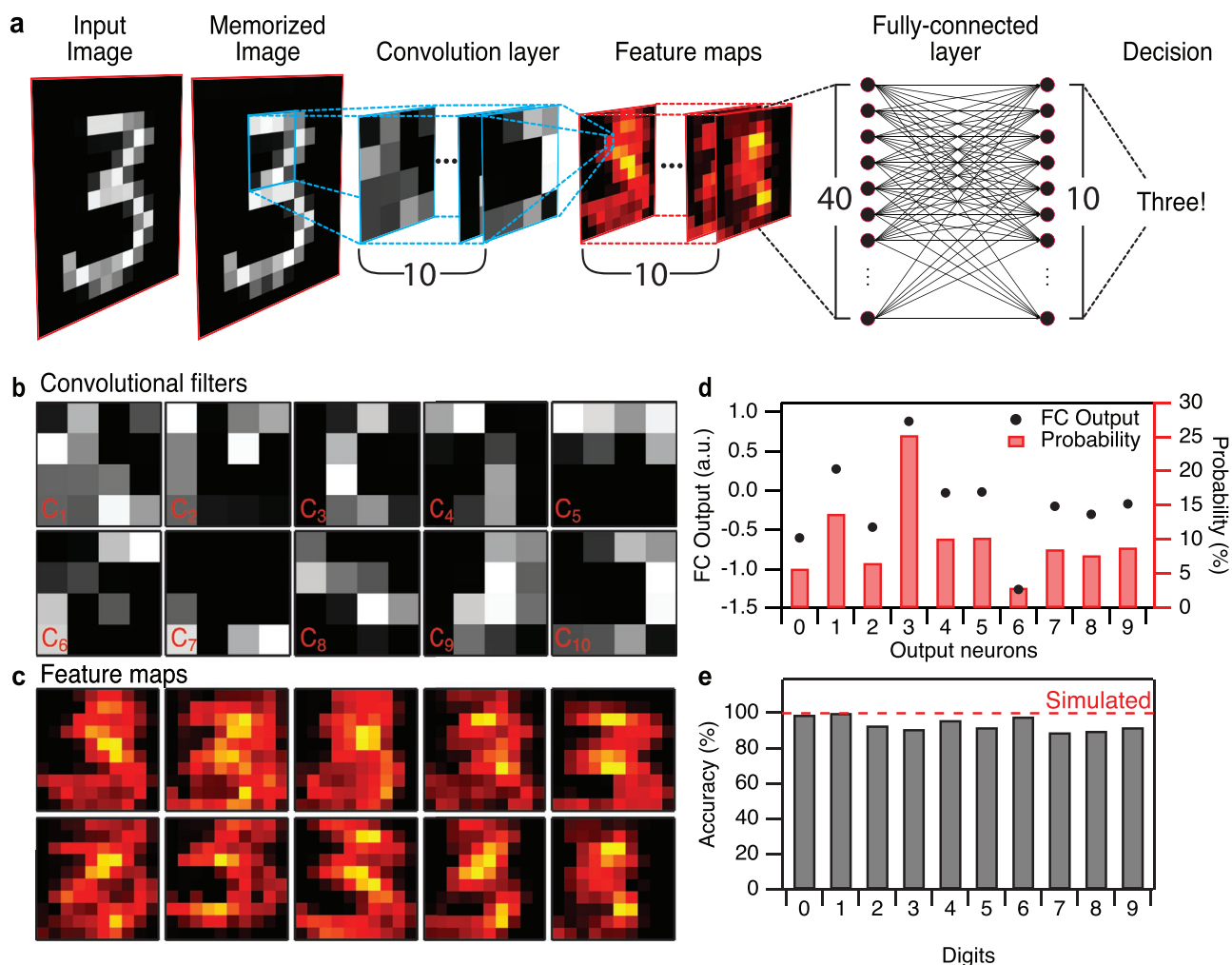


Figure 4. Visual recognition of 1000 hand-written digit images. a) Image sensing and recognition process for an example of hand-written digit “3”, showing the front-end optical–electrical conversion layer for image sensing, the convolution layer to generate feature maps, and the fully connected layer to make a decision. b) Grayscale maps of the ten convolutional filters with each filter represented in 4×4 shape. c) Convolutional layer output feature maps with each feature map of size 10×10 for the input digit “3”. d) Fully connected layer output magnitude (black) and the corresponding Bayesian probabilities (red). e) Visual recognition results for 1000 MNIST images (100 images for each digit of “0” to “9”) using the crossbar array. Red dashed line indicates the recognition accuracy performed in the software domain.

Supporting Information

Supporting Information is available from the Wiley Online Library or from the author.

Acknowledgements

The authors acknowledge the support by Samsung Advanced Institute of Technology (SAIT) on the collaborative research for the two-dimensional materials and their applications (A30216), and the support by the National Science Foundation (NSF) on the Science and Technology Center for Integrated Quantum Materials (DMR-1231319) and on the research project for quantum optoelectronics, magnetoelectronics and plasmonics in 2-dimensional materials heterostructures (EFMA-1542807). Device fabrication was performed in part at the Harvard Center for Nanoscale Systems (CNS), which is supported by the NSF under Contract 1541959.

Conflict of Interest

The authors declare no conflict of interest.

Author Contributions

H.J. and C.L. contributed equally to this work. H.J., C.L., D.H., and S.P. conceived the project. H.J., C.L., H.H., and D.H. designed the 2D ICs, and H.J. and M.-H.L. fabricated them. H.J., C.L., and H.H. developed the measurement system and performed the measurements. H.J., C.L., H.H., and D.H. analyzed the data. H.K., M.S., H.S., and S.P. synthesized 2D materials. H.J., C.L., H.H., S.P., and D.H. wrote the paper. D.H. and S.P. supervised the project. All authors discussed the results and implications, and reviewed the manuscripts.

Keywords

2D materials, crossbar arrays, integrated circuits, neural networks, transition metal dichalcogenides

Received: April 8, 2020
Revised: June 13, 2020
Published online: July 23, 2020

- [1] K. S. Novoselov, A. Mishchenko, A. Carvalho, A. H. C. Neto, *Science* **2016**, 353, aac9439.
- [2] S. Manzeli, D. Ovchinnikov, D. Pasquier, O. V. Yazyev, A. Kis, *Nat. Rev. Mater.* **2017**, 2, 17033.
- [3] Q. H. Wang, K. Kalantar-Zadeh, A. Kis, J. N. Coleman, M. S. Strano, *Nat. Nanotechnol.* **2012**, 7, 699.
- [4] C.-H. Lee, G.-H. Lee, A. M. van der Zande, W. Chen, Y. Li, M. Han, X. Cui, G. Arefe, C. Nuckolls, T. F. Heinz, J. Guo, J. Hone, P. Kim, *Nat. Nanotechnol.* **2014**, 9, 676.
- [5] Y. Wang, E. Liu, A. Gao, T. Cao, M. Long, C. Pan, L. Zhang, J. Zeng, C. Wang, W. Hu, S.-J. Liang, F. Miao, *ACS Nano* **2018**, 12, 9513.
- [6] V. K. Sangwan, D. Jariwala, I. S. Kim, K.-S. Chen, T. J. Marks, L. J. Lauhon, M. C. Hersam, *Nat. Nanotechnol.* **2015**, 10, 403.
- [7] R. Xu, H. Jang, M.-H. Lee, D. Amanov, Y. Cho, H. Kim, S. Park, H. Shin, D. Ham, *Nano Lett.* **2019**, 19, 2411.
- [8] F. Zhou, J. Chen, X. Tao, X. Wang, Y. Chai, *Research* **2019**, 2019, 9490413.
- [9] G. Fiori, F. Bonaccorso, G. Iannaccone, T. Palacios, D. Neumaier, A. Seabaugh, S. K. Banerjee, L. Colombo, *Nat. Nanotechnol.* **2014**, 9, 768.
- [10] J.-W. T. Seo, J. Zhu, V. K. Sangwan, E. B. Secor, S. G. Wallace, M. C. Hersam, *ACS Appl. Mater. Interfaces* **2019**, 11, 5675.
- [11] B. Radisavljevic, A. Kis, *Nat. Mater.* **2013**, 12, 815.
- [12] O. Lopez-Sanchez, D. Lembke, M. Kayci, A. Radenovic, A. Kis, *Nat. Nanotechnol.* **2013**, 8, 497.
- [13] K. Kang, S. Xie, L. Huang, Y. Han, P. Y. Huang, K. F. Mak, C.-J. Kim, D. Muller, J. Park, *Nature* **2015**, 520, 656.
- [14] T. Kim, J. Mun, H. Park, D. Joung, M. Diware, C. Won, J. Park, S.-H. Jeong, S.-W. Kang, *Nanotechnology* **2017**, 28, 18LT01.
- [15] Y.-H. Lee, L. Yu, H. Wang, W. Fang, X. Ling, Y. Shi, C.-T. Lin, J.-K. Huang, M.-T. Chang, C.-S. Chang, M. Dresselhaus, T. Palacios, L.-J. Li, J. Kong, *Nano Lett.* **2013**, 13, 1852.
- [16] W. Lee, Y. Liu, Y. Lee, B. K. Sharma, S. M. Shinde, S. D. Kim, K. Nan, Z. Yan, M. Han, Y. Huang, Y. Zhang, J.-H. Ahn, J. A. Rogers, *Nat. Commun.* **2018**, 9, 1417.
- [17] L. Yu, D. El-Damak, U. Radhakrishna, X. Ling, A. Zubair, Y. Lin, Y. Zhang, M.-H. Chuang, Y.-H. Lee, D. Antoniadis, J. Kong, A. Chandrakasan, T. Palacios, *Nano Lett.* **2016**, 16, 6349.
- [18] L. Yu, A. Zubair, E. Santos, X. Zhang, Y. Lin, *Nano Lett.* **2015**, 15, 4928.
- [19] S. Wachter, D. K. Polyushkin, O. Bethge, T. Mueller, *Nat. Commun.* **2017**, 8, 14948.
- [20] W. Zhang, J.-K. Huang, C.-H. Chen, Y.-H. Chang, Y.-J. Cheng, L.-J. Li, *Adv. Mater.* **2013**, 25, 3456.
- [21] J. Lee, S. Pak, Y.-W. Lee, Y. Cho, J. Hong, P. Giraud, H. S. Shin, S. M. Morris, J. I. Sohn, S. Cha, J. M. Kim, *Nat. Commun.* **2017**, 8, 14734.
- [22] H. Fang, W. Hu, *Adv. Sci.* **2017**, 4, 1700323.
- [23] M. M. Furchi, D. K. Polyushkin, A. Pospischil, T. Mueller, *Nano Lett.* **2014**, 14, 6165.
- [24] C. Li, M. Hu, Y. Li, H. Jiang, N. Ge, E. Montgomery, J. Zhang, W. Song, N. Dávila, C. E. Graves, Z. Li, J. P. Strachan, P. Lin, Z. Wang, M. Barnell, Q. Wu, R. S. Williams, J. J. Yang, Q. Xia, *Nat. Electron.* **2017**, 1, 52.
- [25] P. M. Sheridan, F. Cai, C. Du, W. Ma, Z. Zhang, W. D. Lu, *Nat. Nanotechnol.* **2017**, 12, 784.
- [26] M. Hu, C. E. Graves, C. Li, Y. Li, N. Ge, E. Montgomery, N. Davila, H. Jiang, R. S. Williams, J. J. Yang, Q. Xia, J. P. Strachan, *Adv. Mater.* **2018**, 30, 1705914.
- [27] Z. Wang, C. Li, W. Song, M. Rao, D. Belkin, Y. Li, P. Yan, H. Jiang, P. Lin, M. Hu, J. P. Strachan, N. Ge, M. Barnell, Q. Wu, A. G. Barto, Q. Qiu, R. S. Williams, Q. Xia, J. J. Yang, *Nat. Electron.* **2019**, 2, 115.
- [28] M. A. Zidan, J. P. Strachan, W. D. Lu, *Nat. Electron.* **2018**, 1, 22.
- [29] S. Ambrogio, P. Narayanan, H. Tsai, R. M. Shelby, I. Boybat, C. di Nolfo, S. Sidler, M. Giordano, M. Bodini, N. C. P. Farinha, B. Killeen, C. Cheng, Y. Jaoudi, G. W. Burr, *Nature* **2018**, 558, 60.
- [30] F. Zhou, Z. Zhou, J. Chen, T. H. Choy, J. Wang, N. Zhang, Z. Lin, S. Yu, J. Kang, H.-S. P. Wong, Y. Chai, *Nat. Nanotechnol.* **2019**, 14, 776.
- [31] J. Xue, Z. Zhu, X. Xu, Y. Gu, S. Wang, L. Xu, Y. Zou, J. Song, H. Zeng, Q. Chen, *Nano Lett.* **2018**, 18, 7628.
- [32] S. Gao, G. Liu, H. Yang, C. Hu, Q. Chen, G. Gong, W. Xue, X. Yi, J. Shang, R.-W. Li, *ACS Nano* **2019**, 13, 2634.
- [33] S. Chen, Z. Lou, D. Chen, G. Shen, *Adv. Mater.* **2018**, 30, 1705400.
- [34] H. Wang, Q. Zhao, Z. Ni, Q. Li, H. Liu, Y. Yang, L. Wang, Y. Ran, Y. Guo, W. Hu, Y. Liu, *Adv. Mater.* **2018**, 30, 1803961.
- [35] Y.-C. Wu, C.-H. Liu, S.-Y. Chen, F.-Y. Shih, P.-H. Ho, C.-W. Chen, C.-T. Liang, W.-H. Wang, *Sci. Rep.* **2015**, 5, 11472.
- [36] A. D. Bartolomeo, L. Genovese, T. Foller, F. Giubileo, G. Luongo, L. Croin, S.-J. Liang, L. K. Ang, M. Schleberger, *Nanotechnology* **2017**, 28, 214002.
- [37] S. Jeon, S.-E. Ahn, I. Song, C. J. Kim, U.-I. Chung, E. Lee, I. Yoo, A. Nathan, S. Lee, K. Ghaffarzadeh, J. Robertson, K. Kim, *Nat. Mater.* **2012**, 11, 301.